ChemPubSoc Europe

DOI: 10.1002/chem.201600857

CHEMISTRY A European Journal Full Paper

Host–Guest Systems |*Hot Paper*|

Looking for the Origin of Allosteric Cooperativity in Metallopolymers

Lucille Babel,[a] Thi Nhu Y Hoang,[a] Laure Guénée,[b] Céline Besnard,[b] Tomasz A. Wesolowski,[c] Marie Humbert-Droz,[c] and Claude Piguet*[a]

Abstract: The basic concept of allosteric cooperativity used in biology, chemistry and physics states that any change in the intermolecular host–guest interactions operating in multisite receptors can be assigned to intersite interactions. Using lanthanide metals as guests and linear multi-tridentate linear oligomers of variable lengths and geometries as hosts, this work shows that the quantitative modeling of metal loadings requires the consideration of a novel phenomenon originating from solvation processes. It stepwise modulates the intrinsic affinity of each isolated site in multisite receptors, and this without resorting to allosteric cooperativity. An easy-to-handle additive model predicts a negative power law dependence of the intrinsic affinity on the length of the linear metallopolymer. Applied to lanthanidopolymers, the latter common analysis overestimates cooperativity factors by more than two orders of magnitude.

Introduction

Metallopolymers are hybrid materials,[1,2] in which metal centers with their specific electronic (optics, magnetism, catalysis) and structural (geometries, coordination numbers) properties are incorporated into organic polymers offering easy processabillity, efficient structural control and rich scalability.[3–5] In view of their promising applications in light-emitting diodes (LED),[6–9] in solid cells for photovoltaics,[10–12] in magnetically active[13] and light-emissive liquid crystals[14,15] and in telecommunication devices,[16,17] the tuning of their properties by a precise and controlled metal-loading of the organic scaffold is clearly underexploited.[18,19] Among the three possible arrangements of the metal complexes with respect to the polymer backbone, often referred to as Wolf-Type I, Type II and Type III (Scheme 1),[20] only the latter, in which the metal centers are incorporated within the polymeric network, have been intensively investigated in the fields of coordination polymers and metal–organic frameworks (MOF).[21–24]

Because of the predetermined optical and magnetic properties associated with their [Xe]4 f^N electronic configurations (N = 0–14), the trivalent lanthanide cations, Ln^{3+}, are attractive metallic partners for the design of application-oriented Type III metallopolymers.[23–26] However, the strict stoichiometry required for the formation of a well-defined polymeric architecture in these systems prevents partial metallic occupancy or heterometallic loading without resorting to doping in random sites.[27,28] On the contrary, the less studied lanthanide-containing metallopolymers belonging to Type I and Type II categories[5] are compatible with the complete or partial filling of the available sites with one or different lanthanide complexes, this without altering the polymeric structures (Figure 1). Polynuclear systems with programmed sequences of (open-shell) metal ions thus become available, a key step to push further ahead with current limits of optical sensing,[29–31] directional light-downshifting[32,33] and energy-transfer light-upconversion.[34] As a starting point for bringing Type I or Type II metallopolymers $\mathbf{L}^N$ within the frame of chemical control, one can benefit from the fact that the thermodynamics of metal load-

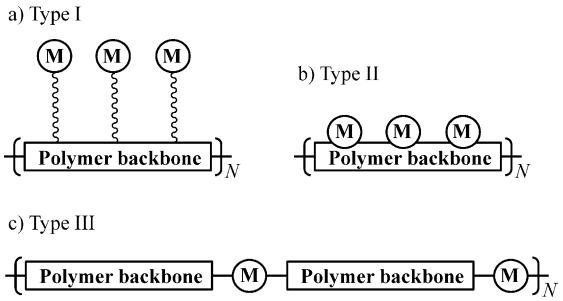

Scheme 1. Wolf Type I–III strategies for the introduction of metal centers into organic polymers.[20] The metal complexes are: a) tethered to the polymer backbone (Type I), b) covalently coupled to the polymer backbone (Type II), and c) integrated as components of the polymer backbone (Type III). For the sake of clarity, only intermolecular metal–ligand binding processes considered in this work are illustrated.

[a] *L. Babel, Dr. T. N. Y. Hoang, Prof. Dr. C. Piguet*
Department of Inorganic, Analytical and Applied Chemistry
University of Geneva, 30 quai E. Ansermet, 1211 Geneva 4 (Switzerland)
E-mail: Claude.Piguet@unige.ch

[b] *Dr. L. Guénée, Dr. C. Besnard*
Laboratory of Crystallography, University of Geneva
24 quai E. Ansermet, 1211 Geneva 4 (Switzerland)

[c] *Prof. Dr. T. A. Wesolowski, M. Humbert-Droz*
Department Physical Chemistry, University of Geneva
30 quai E. Ansermet, 1211 Geneva 4 (Switzerland)

Supporting information for this article can be found under http://dx.doi.org/10.1002/chem.201600857.

ing in these linear metallopolymers is easily caught by a simple model (Figure 1a), which considers only two free energy parameters: the intermolecular affinity $\Delta G_{aff}^{M,L} = -RT\ln\left(f_{aff}^{M,L}\right)$ of a single site for the entering metal, M, in the polymer $\mathbf{L}^N$ and the energetic penalty $\Delta E_{1-2}^{M,M} = -RT\ln\left(u_{1-2}^{M,M}\right) > 0$, or benefit $\Delta E_{1-2}^{M,M} < 0$, produced by a bound site for the fixation of a second metal to an adjacent free site in the polymer $\mathbf{L}^N$.[35] Please note that the associated Boltzmann factor $u_{1-2}^{M,M} = \exp\left(-\Delta E_{1-2}^{M,M}/RT\right)$ is often referred to as the allosteric cooperativity factor in biology, since $u_{1-2}^{M,M} > 1$ or $u_{1-2}^{M,M} < 1$, provides a larger apparent affinity ($\Delta E_{1-2}^{M,M} < 0$, positive cooperativity), respectively, a reduced apparent affinity ($\Delta E_{1-2}^{M,M} > 0$, negative or anti-cooperativity) for successive guest (metal) complexations.[36]

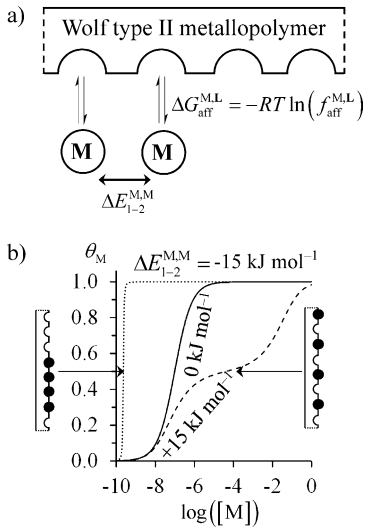

Figure 1. a) Thermodynamic Potts–Ising model for the successive intermolecular connections of metallic units to a one-dimensional multisite receptor $\mathbf{L}^N$ possessing N available binding sites.[35] $\Delta G_{aff}^{M,L} = -RT\ln\left(f_{aff}^{M,L}\right)$ is the non-cooperative free energy of intermolecular connection of one site for the entering metal and $\Delta E_{1-2}^{M,M} = -RT\ln\left(u_{1-2}^{M,M}\right)$ is the free energy of interaction occurring when two adjacent sites are occupied. b) Binding isotherms computed for the metal loading of a linear polymer $\mathbf{L}^N$ ($N \rightarrow \infty$) showing the influence of the nearest-neighbor interaction $\Delta E_{1-2}^{M,M}$ for a fixed value of $\Delta G_{aff}^{M,L} = -40$ kJ mol^{-1}.[37] The pictograms illustrate the dominant microspecies formed for the half-filled Wolf Type II polymer (occupancy factors $\theta_M = 0.5$) upon the operation of positive cooperativity ($\Delta E_{1-2}^{M,M} < 0$, left part, metal clustering) or negative cooperativity ($\Delta E_{1-2}^{M,M} > 0$, right part, metal alternance).

When $\Delta G_{aff}^{M,L}$ and $\Delta E_{1-2}^{M,M}$ are at hand, the average of bound metal per binding site θ_M, which characterizes the filling of the multisite receptor,[35,37,38] can be entirely predicted as a function of the concentration of free metal [Figure 1b and Eq. (5) in part 3].[37] With this in mind, the most appealing linear Type I and II metallopolymers for application-oriented research are those for which: 1) the non-cooperative intrinsic affinity of an isolated site for the metal is large ($f_{aff}^{M,L} \gg 1 \Rightarrow \Delta G_{aff}^{M,L} \ll 0$), and 2) the absolute magnitude of the cooperativity factor is maximized ($\left|u_{1-2}^{M,M}\right| \gg 1$). For large negative cooperativity ($\Delta E_{1-2}^{M,M} \gg RT$), the energetic penalty that the system has to pay for filling two adjacent binding sites in the polymer is so considerable that a plateau develops around $\theta_M = 0.5$ (Figure 1b). A large domain of stability is generated for half-filled polymers, in which every second site is occupied (Figure 1b, right).[37] This ordering phenomenon is analogous to order–disorder phase transition in antiferromagnetic materials and it has been exploited for the formation of organized heteropolymetallic lanthanide complexes.[39] However, a true thermodynamic phase transition is not expected due to the one-dimensional character of the system and its finite size.[40] On the contrary, positive cooperativity, characterized by $\Delta E_{1-2}^{M,M} \ll 0$, results in the formation of clusters of occupied sites for $\theta_M = 0.5$ (Figure 1b, left). The validity of these predictions was recently explored for the design of tunable materials, in which the linear multi-tridentate polymers $\mathbf{L1}^N$ ($N = 10$, 12, 20, 31 is the number of available binding sites, Figure 2a) were loaded with luminescent lanthanide β-diketonates complexes [Ln(hfac)$_3$] (Ln = La, Eu, Y; hfac = hexafluoroacetylacetone).[41,42] Whereas the slightly cooperative ($1.5 \leq u_{1-2}^{Ln,Ln} \leq 1.8$) nearest-neighbor intermetallic interactions accompanying the multistep binding processes leading to [$\mathbf{L1}^N$(Ln(hfac)$_3$)$_m$] do not significantly vary with the polymer length N (red triangles in Figure 2b),[42] the intrinsic affinity f_{aff}^{Ln,L^N} for a specific tridentate binding site drastically decreases by one order of magnitude in going from the monomeric ligand **L0** ($N = 0$) to the polymers $\mathbf{L1}^N$ with $N \geq 10$ (black diamonds in Figure 2b).

The resulting (very) weak intrinsic affinities found for the lanthanide in linear polymers $\mathbf{L1}^N$ is harmful for the efficient and controlled complexation of functional metallic centers along the polymeric strand. In the absence of any understanding of its origin, there is no hope to bring these Wolf-Type II lanthanidopolymers within the field of application. We reasoned that the drastic loss in intrinsic affinity of the tridentate site f_{aff}^{Ln,L^N} observed in the linear polymers $\mathbf{L1}^N$ could be unraveled if the thermodynamic data would be available for $N = 2$ binding sites in the dimeric ligands **L2**–**L4** (green rod in Figure 2b) because the two microscopic parameters $u_{1-2}^{Ln,Ln}$ and f_{aff}^{Ln,L^N} are independent in these systems with no parasitic triplet interactions,[43] a complication which may occur in oligomers possessing more than two binding sites as found in $\mathbf{L1}^N$.[44] We therefore report here on the synthesis and characterization of dimeric ligands **L2**–**L4** showing various relative arrangements of their tridentate N_3 binding sites (Scheme 2). The searched microscopic thermodynamic affinity $f_{aff}^{Ln,Lk}$ and intermetallic interactions $u_{1-2}^{Ln,Ln}$ are deduced from the binding isotherms constructed from ^{1}H and ^{19}F NMR titrations of **L2**–**L4** with [Ln(hfac)$_3$]. Particular efforts are focused on the implementation of a simple and predictive model for catching the reliable intrinsic affinities and allosteric cooperativity factors, which operate in linear metallopolymers and, by extension, in multisite receptors exploited in materials science.

Experimental Section

Chemicals were purchased from Strem, Acros, Fluka AG, and Aldrich, and were used without further purification unless otherwise stated. The unsymmetrical tridentate unit **1** was prepared in 11% global yield according to an improved literature procedure, then

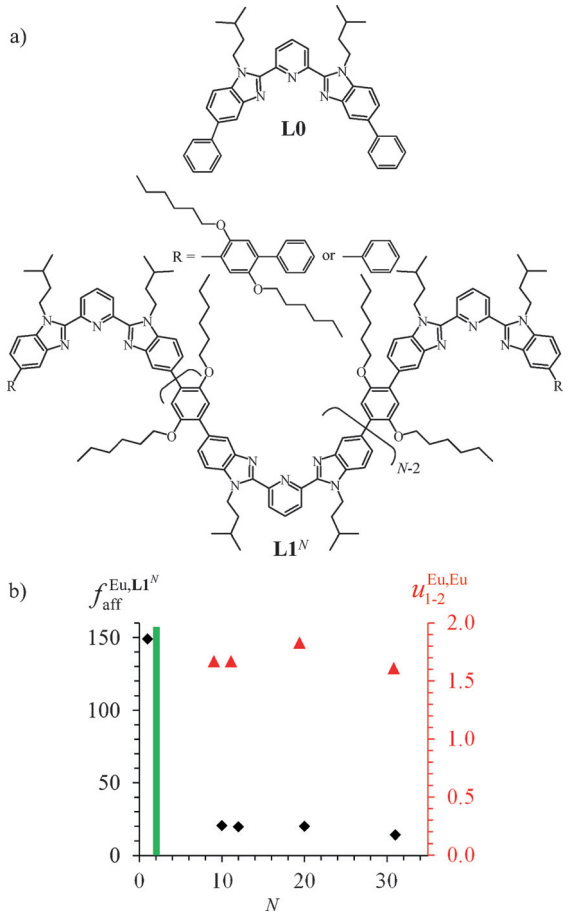

Figure 2. a) Chemical structure of the monomeric tridentate binding unit **L0** found in the multi-tridentate polymers **L1**^{N}. b) Intrinsic affinities for a single binding site $f_{aff}^{Eu,L1^N}$ (black diamonds, left scale) and cooperativity factors $u_{1-2}^{Eu,Eu}$ (red triangles, right scale) reported for the loading of oligomers **L1**^{N} (N = 10–31) with [Eu(hfac)$_3$(diglyme)] (CD_2Cl_2, 298 K).[42] The vertical green rod indicates the crucial missing data for a dimeric receptor.

transformed into its boronic ester **2** by using a standard procedure (Appendix 1 in the Supporting Information).[45] The preparation of the boronic ester **2** and boronic acids **3**–**5** are collected in Appendix 2 (Supporting Information). The hexafluoroacetylacetonate salts [Ln(hfac)$_3$(diglyme)] were prepared from the corresponding oxide (Appendix 2).[46,47] DMF and dichloromethane were distilled over calcium hydride. Silica gel plates Merck 60 F254 were used for thin layer chromatography (TLC) and Fluka silica gel 60 (0.04–0.063 mm) was used for preparative column chromatography.

Synthesis and characterization

Preparation of 5,5′-(2,5-bis(hexyloxy)-1,4-phenylene)bis(1-isopentyl-2-(6-(1-isopentyl-5-phenyl-1*H*-benzo[*d*]imidazol-2-yl)pyridin-2-yl)-1*H*-benzo[*d*]imidazole) (L2): 2,5-Dihexyloxy-1,4-phenylenediboronic acid (**3**, 178 mg, 0.49 mmol, 1.0 equiv), 5-bromo-1-isopentyl-2-(6-(1-isopentyl-5-phenyl-1*H*-benzo[*d*]imidazol-2-yl)pyridin-2-yl)-1*H*-benzo[d]imidazole (**1**, 677 mg, 1.12 mmol, 2.2 equiv), CsF (370 mg, 2.44 mmol, 5.0 equiv) and tetrakis(triphenylphosphine)-palladium(0) (56 mg, 0.05 mmol, 0.1 equiv) were introduced into a Schlenk tube, which was flushed with argon. A degassed mixture of dioxane (8 mL) and ethanol (3 mL) was added, and the mixture was heated at 100 °C for 48 h under an inert atmosphere. After evaporation to dryness, the solid was partitioned between sat. NaCl (150 mL) and dichloromethane (100 mL). The aq. phase was extracted with dichloromethane (2×150 mL). The combined organic phases were dried over Na_2SO_4, filtered and evaporated to dryness. The solid was purified by column chromatography (Silicagel, CH_2Cl_2/MeOH, 100:0→97:3) to obtain a brown solid, which was recrystallized from EtOH/CH_2Cl_2 to yield **L2** (394 mg, 61 %) as a white powder. ^{1}H NMR (400 MHz, $CDCl_3$): δ = 8.40 (dd, J = 8.0, 0.9 Hz, 2H), 8.38 (dd, J = 8.0, 0.9 Hz, 2H), 8.17 (d, J = 1.0 Hz, 2H), 8.14 (d, J = 0.9 Hz, 2H), 8.12 (t, J = 6.8 Hz, 2H), 7.78 (dd, J = 8.4, 1.4 Hz, 2H), 7.76–7.71 (m, 4H), 7.67 (dd, J = 8.4, 1.6 Hz, 2H), 7.56 (d, J = 8.1 Hz, 2H), 7.55 (d, J = 8.4 Hz, 2H), 7.51 (t, J = 7.8 Hz, 4H), 7.39 (tt, J = 7.7, 1.1 Hz, 2H), 7.21 (s, 2H), 4.81 (t, J = 6.8 Hz, 8H), 4.04 (t, J = 6.6 Hz, 4H), 1.84–1.66 (m, 12H), 1.57–1.38 (m, 8H), 1.37- 1.27 (m, 8H), 0.89 (t, J = 6.7 Hz, 6H), 0.79 ppm (d, J = 6.6 Hz, 24H); ^{13}C NMR (101 MHz, $CDCl_3$): δ = 150.81 (2 C_{quat}), 150.38 (2 C_{quat}), 150.33 (2 C_{quat}), 150.11 (2 C_{quat}), 149.93 (2 C_{quat}), 143.45 (2 C_{quat}), 142.96 (2 C_{quat}), 141.74 (2 C_{quat}), 138.23 (2 CH), 136.47 (2 C_{quat}), 135.74 (2 C_{quat}), 135.40 (2 C_{quat}), 133.52 (2 C_{quat}), 130.98 (2 C_{quat}), 128.85 (4 CH), 127.44 (4 CH), 126.90 (2 CH), 125.99 (2 CH), 125.57 (2 CH), 125.47 (2 CH), 123.39 (2 CH), 120.98 (2 CH), 118.69 (2 CH), 116.87 (2 CH), 110.43 (2 CH), 109.39 (2 CH), 69.77 (2 CH_2), 43.62 (4 CH_2), 38.93 (4 CH_2), 31.52 (2 CH_2), 29.40 (2 CH_2), 25.87 (2 CH), 25.83 (2 CH), 25.78 (2 CH_2), 22.61 (2 CH_2), 22.26 (4 CH_3), 22.24 (4 CH_3), 14.03 ppm (2 CH_3); ESI-MS (positive mode, CH_3OH/$CHCl_3$/0.1 % formic acid, $C_{88}H_{100}N_{10}O_2$, M_W = 1329.8 g mol^{-1}): m/z 666.0 ([M+2H]$^{2+}$), 1330.8 ([M+H]$^+$); elemental analyses calcd for $C_{88}H_{100}N_{10}O_2$, C 79.48, H 7.58, N 10.53; found C 79.45, H 7.63, N 10.47.

The same procedure was followed for the preparation of **L2a** from **1** and **3a** (yield 50 %), and for the preparation of **L3** from **1** and **4** (63 %).

L2a: ^{1}H NMR (400 MHz, CD_2Cl_2): δ = 8.40 (dd, J = 7.8, 0.8 Hz, 2H), 8.38 (dd, J = 7.9, 0.9 Hz, 2H), 8.18 (d, J = 1.2 Hz, 2H), 8.13 (d, J = 1.4 Hz, 2H), 8.12 (t, J = 7.9 Hz, 2H), 7.71–7.76 (m, 6H), 7.67 (dd, J = 8.4, 1.6 Hz, 2H), 7.57 (d, J = 8.1 Hz, 2H), 7.56 (d, J = 8.5 Hz, 2H), 7.51 (t, J = 7.7 Hz, 4H), 7.39 (t, J = 7.4 Hz, 2H), 7.20 (s, 2H), 4.81 (t, J = 7.6 Hz, 8H), 3.91 (s, 6H), 1.77–1.66 (m, 8H), 1.57–1.42 (m, 4H), 0.79 (d, J = 6.6 Hz, 12H), 0.78 ppm (d, J = 6.6 Hz, 12H); ESI-MS (positive mode, CH_3OH/$CHCl_3$/0.1 % formic acid, $C_{78}H_{80}N_{10}O_2$, M_W = 1189.6 g mol^{-1}): m/z 595.8 ([M+2H]$^{2+}$), 1190.3 ([M+H]$^+$); elemental analysis calcd for $C_{78}H_{80}N_{10}O_2$·0.1 CH_2Cl_2, C 78.14, H 6.74, N 11.66; found C 78.12, H 6.82, N 11.73; the trace of dichloromethane found in the bulk solid could be detected as a weak singlet at δ = 5.30 ppm when the ^{1}H NMR spectrum was recorded in $CDCl_3$.

L3: ^{1}H NMR (400 MHz, $CDCl_3$): δ = 8.36 (d, J = 7.8 Hz, 2H), 8.35 (d, J = 7.9 Hz, 2H), 8.11 (d, J = 1.1 Hz, 4H), 8.10 (t, J = 7.9 Hz, 2H), 7.72 (d, J = 7.2 Hz, 4H), 7.65 (dd, J = 8.4, 1.8 Hz, 4H), 7.57 (d, J = 8.2 Hz, 2H), 7.53 (s, 1H), 7.51 (t, J = 7.7 Hz, 4H), 7.47 (d, J = 8.3 Hz, 2H), 7.39 (t, J = 7.4 Hz, 2H), 6.77 (s, 1H), 4.88–4.69 (m, 8H), 4.10 (t, J = 6.6 Hz, 4H), 1.83 (p, J = 6.7 Hz, 4H), 1.69 (dt, J = 6.4, 5.9 Hz, 8H), 1.55–1.41 (m, 8H), 1.39–1.27 (m, 8H), 0.89 (t, J = 6.9 Hz, 6H), 0.76 ppm (d, J = 6.6 Hz, 24H); ^{13}C NMR (101 MHz, CD_2Cl_2): δ = 156.15 (2 C_{quat}), 150.91 (2 C_{quat}), 150.28 (4 C_{quat}), 149.99 (2 C_{quat}), 143.58 (2 C_{quat}), 143.06 (2 C_{quat}), 141.69 (2 C_{quat}), 138.02 (2 CH), 135.99 (2 C_{quat}), 135.94 (2 C_{quat}), 135.23 (2 C_{quat}), 133.31 (CH), 133.12 (2 C_{quat}), 128.78 (4 CH), 127.28 (4 CH), 126.81 (2 CH), 125.67 (2 CH), 125.40 (2 CH), 125.25 (2 CH), 123.76 (2 C_{quat}), 122.95 (2 CH), 120.70 (2 CH), 118.32 (2 CH), 110.55 (2 CH), 109.43 (2 CH), 98.73 (CH), 68.96 (2 CH_2), 43.62 (2 CH_2), 43.56 (2 CH_2), 38.82 (4 CH_2), 31.53 (2 CH_2), 29.27 (2 CH_2), 25.84 (2 CH), 25.81 (2 CH), 25.78 (2 CH_2), 22.60 (2 CH_2), 21.95 (4 CH_3), 13.80 ppm (2 CH_3); ESI-MS (positive mode, CH_3OH/$CHCl_3$/0.1 % formic acid, $C_{88}H_{100}N_{10}O_2$, M_W = 1329.8 g mol^{-1}): m/z 666.0 ([M+2H]$^{2+}$), 1330.8 ([M+H]$^+$); elemental analysis calcd

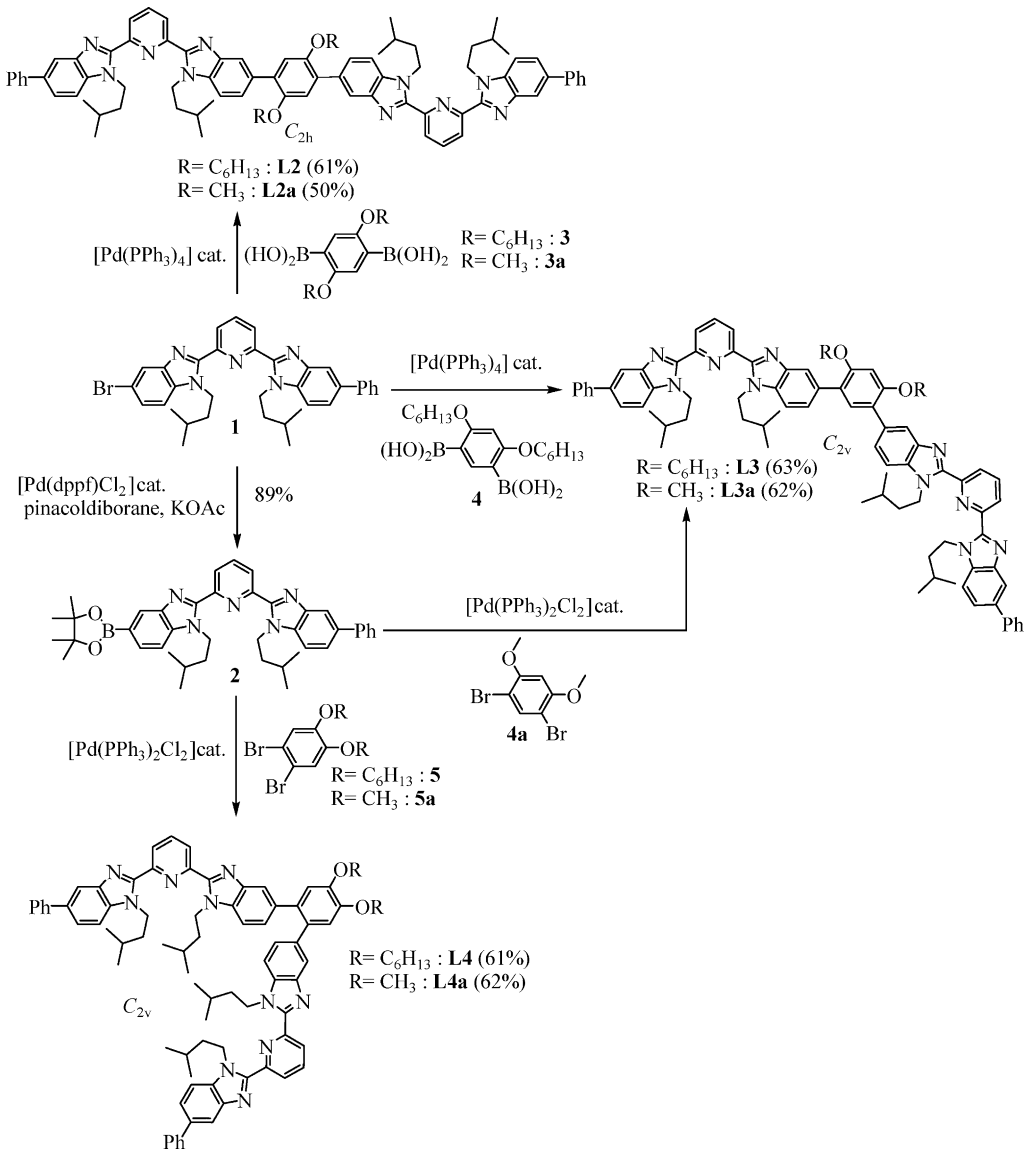

Scheme 2. Synthesis of ligands **L2**–**L4** and of their non-lipophilic analogues **L2a**–**L4a**. The chemical structures and their point groups are those established by ^{1}H and ^{13}C NMR spectroscopy in solution.

for $C_{88}H_{100}N_{10}O_2$, C 79.48, H 7.58, N 10.53; found C 79.05, H 7.59, N 10.45.

Preparation of 5,5′-(4,5-bis(hexyloxy)-1,2-phenylene)bis(1-isopentyl-2-(6-(1-isopentyl-5-phenyl-1*H*-benzo[*d*]imidazol-2-yl)pyridin-2-yl)-1*H*-benzo[*d*]imidazole) (L4): A solution of 1-isopentyl-2-(6-(1-isopentyl-5-(4,4,5,5-tetramethyl-1,3,2-dioxaborolan-2-yl)-1*H*-benzo[*d*]imidazol-2-yl)pyridin-2-yl)-5-phenyl-1*H*-benzo[*d*]imidazole (**2**, 625 mg, 0.65 mmol, 2.5 equiv) in dioxane (15 mL) was introduced into a Schlenk tube containing 1,2-dibromo-4,5-bis(hexyloxy)benzene (167 mg, 0.38 mmol), bis(triphenylphosphine)palladium(II) dichloride (53 mg, 0.08 mmol, 0.2 equiv) and K_2CO_3 (211 mg, 1.53 mmol, 5.0 equiv) under an inert atmosphere. Water (1.3 mL) was added into the Schlenk and the mixture heated at reflux for 48 h under argon. After evaporation to dryness, the solid was partitioned between half sat. $NaHCO_3$ (200 mL) and dichloromethane (200 mL). The aq. phase was extracted with dichloromethane (2× 200 mL). The combined organic phases were dried over Na_2SO_4, filtered and evaporated to dryness. The solid was purified by column chromatography (Silicagel, CH_2Cl_2/MeOH, 100:0→98:2) to yield **L4** as a pale brown solid (311 mg, 61%). ^{1}H NMR (400 MHz, $CDCl_3$): $\delta =$ 8.23 (dd, $J=4.2$, 0.9 Hz, 2H), 8.21 (dd, $J=3.3$, 1.0 Hz, 2H), 7.99 (s, 2H), 7.97 (t, $J=7.8$ Hz, 2H), 7.75 (d, $J=1.0$ Hz, 2H), 7.66–7.57 (m, 4H), 7.53 (dd, $J=8.5$, 1.6 Hz, 2H), 7.42 (d, $J=8.0$ Hz, 2H), 7.39 (t, $J=7.9$ Hz, 4H), 7.27 (tt, $J=4.2$, 0.9 Hz, 2H), 7.11 (d, $J=8.5$ Hz, 2H), 7.04 (dd, $J=8.5$, 1.5 Hz, 2H), 7.02 (s, 2H), 4.65 (t, $J=7.4$ Hz, 4H), 4.58 (t, $J=7.6$ Hz, 4H), 4.04 (t, $J=6.7$ Hz, 4H), 1.81 (quin, $J=6.7$ Hz, 4H), 1.29–1.49 (m, 8H), 1.49–1.40 (m, 4H), 1.34–1.25 (m, 12H), 0.85 (t, $J=7.1$ Hz, 6H), 0.63 (d, $J=6.6$ Hz, 12H), 0.60 ppm (d, $J=6.6$ Hz, 12H); ^{13}C NMR (101 MHz, $CDCl_3$): $\delta =$ 150.83 (2 C_{quat}), 150.15 (2 C_{quat}), 150.04 (2 C_{quat}), 149.88 (2 C_{quat}), 148.30 (2 C_{quat}), 143.41 (2 C_{quat}), 142.88 (2 C_{quat}), 141.70 (2 C_{quat}), 138.17 (2 CH), 136.90 (2 C_{quat}), 136.44 (2 C_{quat}), 135.66 (2 C_{quat}), 134.88 (2 C_{quat}), 133.36 (2 C_{quat}), 128.83 (4 CH), 127.42 (4 CH), 126.90 (2 CH), 126.60 (2 CH), 125.40 (2 CH), 123.36 (2 CH), 121.21 (2 CH), 118.66 (2 CH), 116.79 (2 CH), 110.39 (2 CH), 109.35 (2 CH), 69.47 (2 CH_2), 43.57 (2 CH_2), 43.50 (2 CH_2), 38.84 (2 CH_2), 38.81 (2 CH_2), 31.63 (2 CH_2), 29.35 (2 CH_2), 25.81 (2 CH), 25.77 (2 CH_2), 25.70 (2 CH), 22.67 (2 CH_2), 22.24 (4 CH_3), 22.17 (4 CH_3), 14.07 ppm (2 CH_3); ESI-MS (positive mode, CH_3OH/

$CHCl_3$/0.1% formic acid, $C_{88}H_{100}N_{10}O_2$, $M_W = 1329.8\ g\,mol^{-1}$): *m/z* 1330.8 ($[M+H]^+$); elemental analysis calcd for $C_{88}H_{100}N_{10}O_2 \cdot 0.2\,CH_2Cl_2$, C 78.52, H 7.50, N 10.38; found C 78.55, H 7.65, N 10.12; the trace of dichloromethane found in the bulk solid could be detected as a weak singlet at $\delta = 5.30$ ppm when the ^{1}H NMR spectrum was recorded in $CDCl_3$.

The same procedure was followed for the preparation of **L3a** from **2** and **4a** (yield 62%), and for the preparation of **L4a** from **2** and **5a** (62%).

L3a: ^{1}H NMR (400 MHz, $CDCl_3$): $\delta = 8.35$ (d, $J = 7.3$ Hz, 2H), 8.33 (d, $J = 7.3$ Hz, 2H), 8.11 (d, $J = 1.2$ Hz, 2H), 8.09 (d, $J = 1.3$ Hz, 2H), 8.08 (t, $J = 7.9$ Hz, 2H), 7.70 (d, $J = 7.3$ Hz, 4H), 7.63 (dd, $J = 8.4$, 1.2 Hz, 2H), 7.60 (dd, $J = 8.2$, 1.2 Hz, 2H), 7.55 (s, 1H), 7.52 (d, $J = 8.8$ Hz, 2H), 7.49 (t, $J = 8.0$ Hz, 4H), 7.49 (d, $J = 8.4$ Hz, 2H), 7.37 (t, $J = 7.4$ Hz, 2H), 6.77 (s, 1H), 4.81–4.71 (m, 8H), 3.96 (s, 6H), 1.71–1.61 (m, 8H), 0.89 (dsept, $J = 6.8$, 2.0 Hz, 4H), 0.75 (d, $J = 5.8$ Hz, 12H), 0.73 ppm (d, $J = 5.8$ Hz, 12H); ESI-MS (positive mode, $CH_3OH/CHCl_3$: 0.1% formic acid, $C_{78}H_{80}N_{10}O_2$, $M_W = 1189.6\ g\,mol^{-1}$): *m/z* 1190.3 ($[M+H]^+$).

L4a: ^{1}H NMR (400 MHz, $CDCl_3$): $\delta = 8.30$ (d, $J = 7.8$ Hz, 2H), 8.30 (d, $J = 7.9$ Hz, 2H), 8.07 (d, $J = 1.3$ Hz, 2H), 8.05 (t, $J = 7.9$ Hz, 2H), 7.83 (d, $J = 1.2$ Hz, 2H), 7.69 (d, $J = 7.3$ Hz, 4H), 7.61 (dd, $J = 8.5$, 1.6 Hz, 2H), 7.50 (d, $J = 8.4$ Hz, 2H), 7.47 (t, $J = 7.7$ Hz, 4H), 7.36 (t, $J = 7.4$ Hz, 2H), 7.20 (d, $J = 8.5$ Hz, 2H), 7.13 (dd, $J = 8.4$, 1.4 Hz, 2H), 7.09 (s, 2H), 4.73 (t, $J = 7.6$ Hz, 4H), 4.66 (t, $J = 7.6$ Hz, 4H), 3.99 (s, 6H), 1.69-1.55 (m, 8H), 1.46–1.32 (m, 4H), 0.70 (d, $J = 6.6$ Hz, 12H), 0.67 ppm (d, $J = 6.6$ Hz, 12H); ESI-MS (positive mode, $CH_3OH/CHCl_3$/0.1% formic acid, $C_{78}H_{80}N_{10}O_2$, $M_W = 1189.6\ g\,mol^{-1}$): *m/z* 1190.3 ($[M+H]^+$).

Preparation of the X-ray quality prims for the complexes $[Ln_2(Lk)(hfac)_6]$ (Ln = Eu, Er and k = 2, 2a, 3a, 4a): In a typical procedure, **Lk** (0.006 mmol) and $[Ln(hfac)_3diglyme]$ (0.013 mmol) were dissolved and stirred in dichloromethane/acetonitrile or chloroform/acetonitrile mixtures (ca. 1–2 mL) for 1 h. Slow diffusion of volatile ethers (diethylether or diisopropylether) yielded yellow crystals of $[\mathbf{L2a}Eu_2(hfac)_6]\cdot 3.5\,CHCl_3$ (**6**), $[\mathbf{L3a}Eu_2(hfac)_6]\cdot 1.764\,CH_3CN$ (**7**), $[\mathbf{L4a}Eu_2(hfac)_6]$ (**8**), $[L2Eu_2(hfac)_6]\cdot 2\,CH_2Cl_2$ (**9**) and $[L2Er_2(hfac)_6]\cdot 0.5\,CH_3CN\cdot 2\,H_2O$ (**10**) suitable for X-ray diffraction.

Spectroscopic and analytic measurements

^{1}H, ^{19}F and ^{13}C NMR spectra were recorded at 293 K on Bruker Avance 400 MHz. Chemical shifts are given in ppm with respect to tetramethylsilane $Si(CH_3)_4$ for ^{1}H NMR and with C_6F_6 for ^{19}F NMR. Assignments of signals were deduced from COSY, HSQC, HMBC (and NOESY) NMR measurements. Pneumatically assisted electrospray (ESI) mass spectra were recorded from 10^{-4} M solutions on an Applied Biosystems API 150EX LC/MS System equipped with a Turbo Ionspray source®. Elemental analyses were performed by K. L. Buchwalder from the Microchemical Laboratory of the University of Geneva.

X-ray crystallography

Summary of crystal data, intensity measurements and structure refinements for $[\mathbf{L2a}Eu_2(hfac)_6]\cdot 3.5\,CHCl_3$ (**6**), $[\mathbf{L3a}Eu_2(hfac)_6]\cdot 1.764\,CH_3CN$ (**7**), $[\mathbf{L4a}Eu_2(hfac)_6]$ (**8**), $[\mathbf{L2}Eu_2(hfac)_6]\cdot 2\,CH_2Cl_2$ (**9**) and $[\mathbf{L2}Er_2(hfac)_6]\cdot 0.5\,CH_3CN\cdot 2\,H_2O$ (**10**) are collected in Tables S4, S8, S12, S16 and S20 (Supporting Information). Crystals were mounted on a capton loop with protection oil. Cell dimensions and intensities were measured at 180 K on a Supernova (Rigaku) diffractometer with mirror monochromated CuK_α radiation ($\lambda = 1.54184$ Å) and an Atlas CCD camera. Data were corrected for Lorentz and polarization effects and for absorption. The structures were solved by direct methods (SIR,[48] SHELXS[49]) all other calculations were performed with SHELXL,[49] OLEX2[50] and ORTEP[51] programs. CCDC 1436602, 1436603, 1436604, 1436605 and 1436606 contain the supplementary crystallographic data for this paper. These data can be obtained free of charge from The Cambridge Crystallographic Data Centre.

Computational details

The geometry of ligands **L0, L2**, **L3a** and **L4a** as well as the mononuclear complexes $[\mathbf{L0}Ln(hfac)_3]$ (Ln = La, Eu, Y) were optimized at the DFT/B97-D/def2-TZVP level of theory, using the pseudopotential def2-ecp for metal centers.[52,53] Due to the large number of atoms, the geometries of complexes $[\mathbf{L2}Y_x(hfac)_{3x}]$ ($x = 1$ or 2) were optimized at the DFT/B97-D/def SV(P) level of theory, using the pseudopotential def-SV(P) for metal centers. Single point calculations for energy and dipole moments were carried out at the DFT/B97-D/def2-TZVP/def2-ecp level of theory. All calculations were carried out using the Turbomole v6.6 package program.[54]

Results and Discussion

Synthesis of the ligands L2–L4

The Pd^0-catalyzed Miyaura–Suzuki connection of two unsymmetrical tridentate binding units **1** to dialkyloxybenzene boronic acids **3** and **4** gave **L2** and **L3**, respectively.[45] The boronic acid derived from *ortho*-dialkyloxybenzenedibromide **5** could not be obtained and polarity was therefore reversed by the coupling of the tridentate boronic acid **2** with *ortho*-dibromide **5** to give **L4** (Scheme 2).

The observation of twelve ^{1}H NMR signals for the aromatic protons of the two terminal unsymmetrical tridentate 2,6-bis(-benzimidazole)pyridine units in **L2**–**L4** points to the existence of a twofold symmetry for the free ligands in solution (Figure 3 and Figure S1 in the Supporting Information). The detection of enantiotopic pairs (i.e., singlet NMR signals) for the methylene protons of the isopentyl residues (H9 and H9′ in Figure 3) further implies a planar arrangement of the tridentate binding units, thus leading to an average *C2h* point group for **L2** and *C2v* point groups for **L3** and **L4** in solution as illustrated in Scheme 2. Finally, the lack of observable through-space nuclear Overhauser effects (NOEs) between the pyridine protons H2,2′ and the protons of the isopentyl residue (H9,9′) are diagnostic for a standard *trans–trans* arrangement of the three coordinating nitrogen atoms, which minimizes the electrostatic repulsion (Scheme 2 and Figure 3).[45] The poorly soluble non-lipophilic ligands **L2a**–**L4a** have been synthesized for limiting the degrees of freedom during the crystallization processes. They were obtained in fair yields according to the same synthetic strategy (Scheme 2) and display closely related structures in solution (Figure S2).

Thermodynamic metal loading of the ligands L2–L4

The titrations of 5 mM of the dimers **L2**–**L4** with $[Ln(hfac)_3dig]$ (Ln = La, Nd, Sm, Eu, Er, Tm, Lu, Y; hfac = hexafluoroacetylacetonate, dig = diglyme = 1-methoxy-2-(2-methoxyethoxy)-

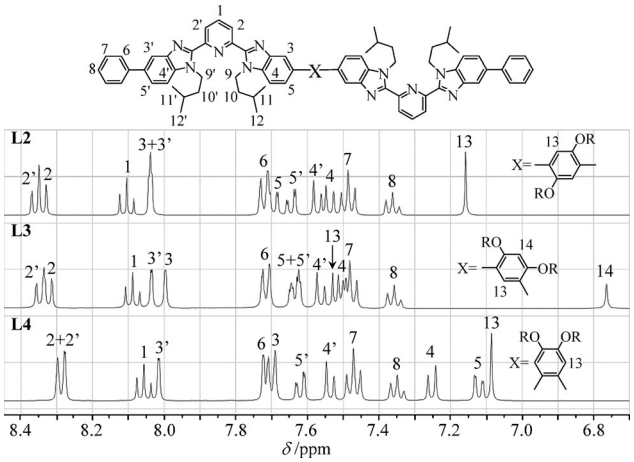

Figure 3. Aromatic part of the ^{1}H NMR spectra of ligands **L2**–**L4** in CD_2CL_2 at 298 K (R = C_6H_{13}).

ethane)[26] in dichloromethane containing an excess of diglyme ($[dig]_{tot}$ = 0.14 M) were monitored by ^{1}H NMR (Figures S3–S5 in the Supporting Information) and ^{19}F NMR (Figure S6) spectroscopy at 298 K. Since the total concentration of diglyme is constant, stability constants $\beta_{exch,m}^{Ln,\mathbf{Lk}}$ characterizing the successive ligand-exchange processes [Eqs. (1) and (2)] reduce to the conditional stability constants $\beta_{cond,m}^{Ln,\mathbf{Lk}}$ summarized in Equations (3) and (4).

$$\mathbf{Lk} + [Ln(hfac)_3(dig)] \rightleftharpoons [\mathbf{Lk}Ln(hfac)_3] + dig \quad \beta_{exch,1}^{Ln,\mathbf{Lk}} = \frac{[\mathbf{Lk}Ln]\cdot[dig]}{[Ln]\cdot[\mathbf{Lk}]} \tag{1}$$

$$\mathbf{Lk} + 2\,[Ln(hfac)_3(dig)] \rightleftharpoons [\mathbf{Lk}Ln_2(hfac)_6] + 2\,dig \quad \beta_{exch,2}^{Ln,\mathbf{Lk}} = \frac{[\mathbf{Lk}Ln_2]\cdot[dig]^2}{[Ln]^2\cdot[\mathbf{Lk}]} \tag{2}$$

$$\beta_{cond,1}^{Ln,\mathbf{Lk}} = \frac{\beta_{exch,1}^{Ln,\mathbf{Lk}}}{[dig]_{tot}} = \frac{[\mathbf{Lk}Ln]}{[Ln]\cdot[\mathbf{Lk}]} = 2f_{aff,cond}^{Ln,\mathbf{Lk}} \tag{3}$$

$$\beta_{cond,2}^{Ln,\mathbf{Lk}} = \frac{\beta_{exch,1}^{Ln,\mathbf{Lk}}}{([dig]_{tot})^2} = \frac{[\mathbf{Lk}Ln_2]}{[Ln]^2\cdot[\mathbf{Lk}]} = \left(f_{aff,cond}^{Ln,\mathbf{Lk}}\right)^2 u_{1-2}^{Ln,Ln} \tag{4}$$

Application of the site-binding model[43] decomposes $\beta_{cond,m}^{Ln,\mathbf{Lk}}$ into a contribution from the conditional intrinsic affinities $f_{aff,cond}^{Ln,\mathbf{Lk}}$ of the tridentate site for the entering $[Ln(hfac)_3]$ metal carrier and an intersite cooperativity factor $u_{1-2}^{Ln,Ln} = exp\left(-\Delta E_{1-2}^{Ln,Ln}/RT\right)$ operating in the saturated complexes $[\mathbf{Lk}Ln_2(hfac)_6]$ [right part of Eqs. (3) and (4)].[41] Since no significant dissociation of the metallic salts occurs in dichloromethane at sub-millimolar concentrations used for NMR titrations,[41] $[Ln(hfac)_3(dig)]$ exists as a single species in solution, the concentration of which is written as [Ln] in Equations (1)–(4), and for the rest of this work. For each $[\mathbf{Lk}]_{tot}/[Ln]_{tot}$ stoichiometric mixture under investigation, the ^{1}H and ^{19}F NMR spectra recorded under thermodynamic equilibrium showed no dynamic exchange process on the NMR time scale (Tables S1 and S2 in the Supporting Information). Consequently, the intensity of the signals of a given nucleus (a proton I^H or a fluorine I^F) in the free ligands **Lk** and in the complexes [Ln], [**Lk**Ln] and [$\mathbf{Lk}Ln_2$] can be exploited for estimating the experimental degree of metalation θ_{Ln}^{exp} [Eq. (5)], from which the concentration of free metal $[Ln] = [Ln]_{tot} - 2\theta_{Ln}[\mathbf{Lk}]_{tot}$ is easily deduced. The plots of θ_{Ln}^{exp} in function of log([Ln]), known as the binding isotherms (Figure 4), are ideally suited for the estimation of $f_{aff,cond}^{Ln,\mathbf{Lk}}$ and $u_{1-2}^{Ln,Ln}$ by using nonlinear least-square fits of θ_{Ln}^{calcd} defined in Equation (6) (Table S3 in the Supporting Information).[41,42]

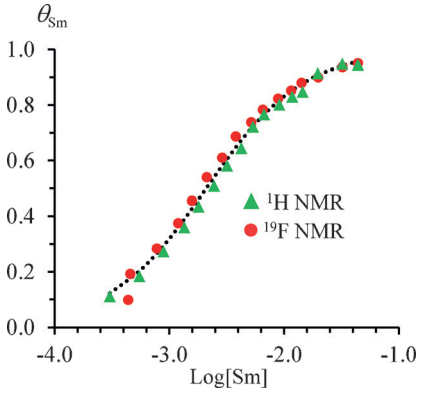

Figure 4. Binding isotherms showing the experimental degree of metalation θ_{Sm} (green triangles for ^{1}H NMR signals, red disks for ^{19}F NMR signals) with respect to the free concentration of metal for the titration of **L2** with $[Sm(hfac)_3dig]$ (CD_2Cl_2 + 0.14 M diglyme at 298 K, Ln = Sm is an arbitrary choice). The dotted black trace corresponds to the binding isotherm fitted with Equation (6) and using $f_{aff,cond}^{Sm,\mathbf{L2}} = 461$ and $u_{1-2}^{Sm,Sm} = 1.10$ (Table S3 in the Supporting Information).

$$\theta_{Ln}^{exp} = \frac{\langle m\rangle}{N} = \frac{1}{2}\frac{|Ln|_{bound}}{|\mathbf{Lk}|_{tot}} = \frac{1}{2}\cdot\frac{I_{\mathbf{LnLk}}^H + 2\left(I_{Ln_2\mathbf{Lk}}^H\right)}{I_{\mathbf{Lk}}^H + I_{\mathbf{LnLk}}^H + I_{Ln_2\mathbf{Lk}}^H} = \frac{I_{\mathbf{LnLk}}^F + I_{Ln_2\mathbf{Lk}}^F}{I_{Ln}^F + I_{\mathbf{LnLk}}^F + I_{Ln_2\mathbf{Lk}}^F}\cdot\frac{[Ln]_{tot}}{2[\mathbf{Lk}]_{tot}} \tag{5}$$

$$\theta_{Ln}^{calcd} = \frac{1}{2}\frac{|Ln|_{bound}}{|\mathbf{Lk}|_{tot}} = \frac{[\mathbf{LnLk}] + 2[Ln_2\mathbf{Lk}]}{2[\mathbf{Lk}]_{tot}} = \frac{1}{2}\left(\frac{2\left(f_{aff,cond}^{Ln,\mathbf{Lk}}\right)[Ln] + 2\left(f_{aff,cond}^{Ln,\mathbf{Lk}}\right)^2\left(u_{1-2}^{Ln,Ln}\right)[Ln]^2}{1 + 2\left(f_{aff,cond}^{Ln,\mathbf{Lk}}\right)[Ln] + \left(f_{aff,cond}^{Ln,\mathbf{Lk}}\right)^2\left(u_{1-2}^{Ln,Ln}\right)[Ln]^2}\right) \tag{6}$$

The experimental cooperativity factors $0.37 \le u_{1-2}^{Ln,Ln} \le 2.59$ do not drastically deviate from $u_{1-2}^{Ln,Ln} = 1$ (Table S3 in the Supporting Information), which stands for a statistical loading of the two tridentate sites of the ligands **L2**–**L4** for the entering metal complexes. Transformed into near-neighbor intersite free energies of interactions $\Delta E_{1-2}^{Ln,Ln} = -RT\ln\left(u_{1-2}^{Ln,Ln}\right)$, we observe that: 1) the most compact ligand **L4** (*ortho*-disubstituted-phenyl spacer, blue trace in Figure 5a) displays a weak cooperative effect, 2) the most extended ligand **L2** (*para*-disubstitut-

ed-phenyl spacer, red trace in Figure 5a) is essentially non-cooperative, and 3) the intermediate ligand **L3** (*meta*-disubstituted-phenyl spacer, green trace in Figure 5a) exhibits minor anti-cooperativity. The weak dependence of $\Delta E_{1-2}^{M,M}$ on the size of the lanthanide cations for **L2** is in line with the drift previously reported for the **L1**^{N} polymers along the La→Eu→Y series.[42]

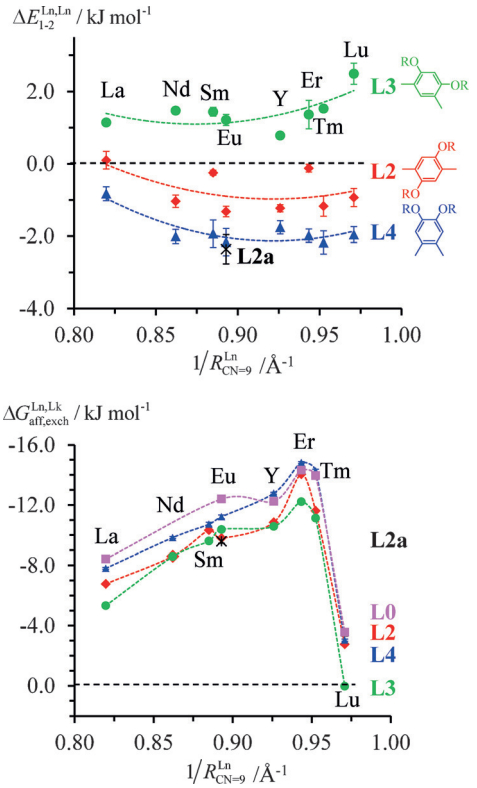

Figure 5. a) Intersite interactions $\Delta E_{1-2}^{Ln,Ln} = -RT\ln(u_{1-2}^{Ln,Ln})$, and b) intrinsic exchange affinities $\Delta G_{aff,exch}^{Ln,Lk} = -RT\ln(f_{aff,cond}^{Ln,Lk} \cdot [dig]_{tot}) = -RT\ln(f_{aff,exch}^{Ln,Lk})$ for the loading of ligands **L0** (magenta), **L2** (red), **L3** (green), **L4** (blue) and **L2a** (black) with [Ln(hfac)$_3$dig] ($1/R_{CN=9}^{Ln}$ is the inverse of nine-coordinate lanthanide radii, CD_2Cl_2, 298 K). The dotted trend-lines are given as guides for the eyes.

The intrinsic exchange affinities of the tridentate site in **L2**–**L4** for the entering lanthanide complex [Eqs. (1) and (2)] can be defined as $\Delta G_{aff,exch}^{Ln,Lk} = -RT\ln(f_{aff,exch}^{Ln,Lk}) = -RT\ln(f_{aff,cond}^{Ln,Lk} \cdot [dig]_{tot})$. They are comparable whatever the choice of the phenyl spacers in **L2**–**L4** and display well-known bell-shaped trends centered around Ln = Er (Figure 5b).[41,42] The most striking result emerges when the exchange affinities $f_{aff,exch}^{Ln,L2}$ observed for the dimer **L2** are compared with those previously collected for the monomer **L0** and for the polymers **L1**^{N} with the same metal (Figure 6). The observation of abrupt negative power dependences of $f_{aff,exch}^{Ln,Lk}$ on the number of available binding sites N shows that the allosteric cooperativity factors $u_{1-2}^{Ln,Ln}$, usually invoked for rationalizing the apparent change in host–guest affinity measured in multisite biological receptors,[38,56,57] are not sufficient for modeling the decreased inclination of the metal for binding a complexation site located in the polymer.

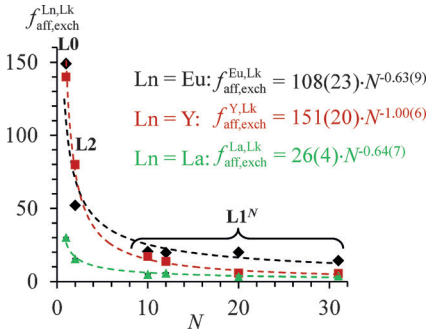

Figure 6. Intrinsic exchange affinity parameters $f_{aff,exch}^{Ln,Lk}$ for the loading of ligands **L0** ($N=1$), **L2** ($N=2$) and **L1**^{N} ($N=10$, 12, 20, 31) with [Ln(hfac)$_3$dig] (N is the number of available tridentate binding sites, CD_2Cl_2, 298 K). The dotted traces were fitted with Equation (13) by using optimized pre-exponential $f_{aff,exch}^{Ln,L0}$ factors.

Behind allosteric cooperativity: the origin of the cooperativity factors

The thermodynamic cycle established for the metal exchange processes $\Delta G_{exch}^{2Ln\rightarrow Ln_2}$ depicted in Scheme 3 is well-suited for comparing the experimental allosteric cooperativity factors $u_{1-2,sol}^{Ln,Ln}$ estimated in solution with their gas-phase analogues $u_{1-2,gas}^{Ln,Ln}$.

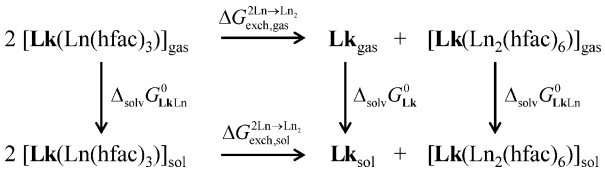

Scheme 3. Thermodynamic cycle for metal exchanges in the dinuclear ligands **L2**–**L4**.

Given that $\Delta G_{exch}^{2Ln\rightarrow Ln_2}$ can be deduced from the conditional stability constants $\Delta G_{exch}^{2Ln\rightarrow Ln_2} = -RT\ln\left(\beta_{cond,2}^{Ln,Lk} \Big/ \left(\beta_{cond,1}^{Ln,Lk}\right)^2\right) = -RT\ln\left(u_{1-2}^{Ln,Ln}/4\right) = \Delta E_{1-2}^{Ln,Ln} + RT\ln(4)$ the Born–Haber cycle can be summarized with Equation (7):

$$\Delta E_{1-2,sol}^{Ln,Ln} = \Delta E_{1-2,gas}^{Ln,Ln} + \Delta_{solv}G^0_{LkLn_2} + \Delta_{solv}G^0_{Lk} - 2\Delta_{solv}G^0_{LkLn} \qquad (7)$$

The experimentally accessible intersite interactions $\Delta E_{1-2,sol}^{Ln,Ln}$ (Figure 5a) can be thus understood as the balance between: 1) an electrostatic contribution arising from the interaction $\Delta E_{1-2,gas}^{Ln,Ln}$ between two "local" dipole moments $\vec{\mu}_1$ and $\vec{\mu}_2$, each taken as that of the monomer [**Lk**Ln(hfac)$_3$] centered on each coordinated metal centers in [**Lk**Ln$_2$(hfac)$_6$] and separated by a distance $R_{Ln\text{-}Ln}$ [Eq. (8), see Figure 8d for an illustration],[61] and 2) the solvation energies $\Delta_{solv}G$ estimated with Equation (9) for **Lk**, [**Lk**Ln(hfac)$_3$] and [**Lk**Ln$_2$(hfac)$_6$] ($N_{Av} = 6.022\times 1023$ mol^{-1} is Avogadro's number, z is the charge of the particle in electrostatic units, $e = 1.602\times10^{-19}$, C is the elementary charge, $\varepsilon_0 = 8.854\times10^{-12}$ C^{2}N^{-1}m^{-2} is the vacuum permittivity, ε_r is the relative dielectric permittivity ($\varepsilon_r = 8.93$ in dichloromethane), μ is the dipole moment of the particle and R_i is the

radius of a spherical cavity cut from the dielectric when a spherical solute is immersed into the solvent).[58–60]

$$\Delta E^{Ln,Ln}_{1-2,gas} = -\frac{N_{av}}{4\pi\varepsilon_0\varepsilon_r}\cdot\left(\frac{\vec{\mu}_1\cdot\vec{\mu}_2}{(R_{Ln-Ln})^3}-3\frac{\left(\vec{\mu}_1\cdot\vec{R}_{Ln-Ln}\right)\left(\vec{\mu}_2\cdot\vec{R}_{Ln-Ln}\right)}{(R_{Ln-Ln})^5}\right) \quad (8)$$

$$\Delta_{solv}G^0 = -N_{av}\frac{\mu^2}{4\pi\varepsilon_0(R_i)^3}\cdot\left(\frac{\varepsilon_r-1}{2\varepsilon_r+1}\right) \quad (9)$$

The numerical evaluation of $\Delta E^{Ln,Ln}_{1-2,gas}$ (Table 1, column 5) and $\Delta_{solv}G^0$ (Table 1, column 6) requires reliable molecular structures for ligands **Lk** and for their complexes [**Lk**Ln$_m$(hfac)$_{3m}$] (m = 1–2). The gas-phase geometries of the monomeric systems **L0** and [**L0**Ln(hfac)$_3$] (Ln = La, Eu, Y, Figure 8a and b) could be easily optimized by using DFT methods, but considerable additional efforts were necessary for getting the same information for the dimeric systems **L2**, **L3a** and **L4a**, [**L2**Y(hfac)$_3$] and [**L2**Y$_2$(hfac)$_6$] (Figure 8c and d). Due to the large number of atoms and the presence of two lanthanides in [**Lk**Ln$_2$(hfac)$_6$], their molecular structures were taken from the crystal structures of [**L2a**Eu$_2$(hfac)$_6$]·3.5 CHCl$_3$ (**6**), [**L3a**Eu$_2$(hfac)$_6$]·1.764 CH$_3$CN (**7**), [**L4a**Eu$_2$(hfac)$_6$] (**8**) and [**L2**Eu$_2$(hfac)$_6$]·(**9**; Figure 7, Tables S4–S23 and Figures S7–S11 in the Supporting Information).

Table 1. Dipole moments (μ_{tot}), intramolecular Ln···Ln distances ($R_{Ln\text{-}Ln}$), hydrodynamic radii (R_i), $\Delta E^{Ln,Ln}_{1-2,gas}$ [Eq. (8)], $\Delta_{solv}G^0$ [Eq. (9)] and $\Delta E^{Ln,Ln}_{1-2,sol}$ [Eq. (7)] computed for ligands **L2**, **L3a** and **L4a** and associated complexes [**Lk**Ln(hfac)$_3$] and [**Lk**Ln$_2$(hfac)$_6$].

Cmpd	μ_{tot} [D][a]	$R_{Ln\text{-}Ln}$ [Å]	R_i[b] [Å]	$\Delta E^{Ln,Ln}_{1-2,gas}$ [kJ mol^{-1}]	$\Delta_{solv}G^0$ [kJ mol^{-1}]	$\Delta E^{Ln,Ln}_{1-2,sol}$ [kJ mol^{-1}]
L2[c]	1.1[d]	–	7.08	–	−0.4[f]	–
	3.7[e]	–	7.13	–		
L3a[c]	3.4[d]	–	6.70	–	−2.0[f]	–
	5.9[e]	–	6.70	–		
L4a[c]	1.5[d]	–	6.73	–	−0.6[f]	–
	4.1[e]	–	6.77	–		
[**L2**Ln(hfac)$_3$] [c]	14.9	–	7.96	–	−11.2	–
[**L3a**Ln(hfac)$_3$]	15.1	–	7.47	–	−13.8	–
[**L4a**Ln(hfac)$_3$]	13.4	–	7.42	–	−11.1	–
[**L2**Ln$_2$(hfac)$_6$] [c]	0.5	15.23	8.60	−0.155	0.0	2
[**L3a**Ln$_2$(hfac)$_6$]	17.0	12.62	8.14	−0.050	−13.5	12.2
[**L4a**Ln$_2$(hfac)$_6$]	26.2	12.52	8.38	0.410	−29.6	−7.3

[a] 1 Debye = 1 D = 3.33564 × 10^{-30} C m. [b] The hydrodynamic radii (R_i) are deduced from the Connolly volumes.[63] [c] Dipole moments computed with DFT/B-97D/def2-TZVP. [d] Dipole moment found for the most stable conformation (Figures 8b and S12). [e] Dipole moment found for the minor conformation (Figures 8b and S12). [f] Solvation energy taken as the weighted sum of those calculated for each accessible conformation.

The dipole moments were computed in the resulting electronic structures (Figure 8, Table 1, column 2),[62] the intersite separations R_{Ln-Ln} were taken as the intermetallic separations in the dinuclear complexes (Table 1, column 3) and the size of the solvated cavities R_i were approximated as the hydrodynamic radii of the incriminated species (Table 1, column 4).[63]

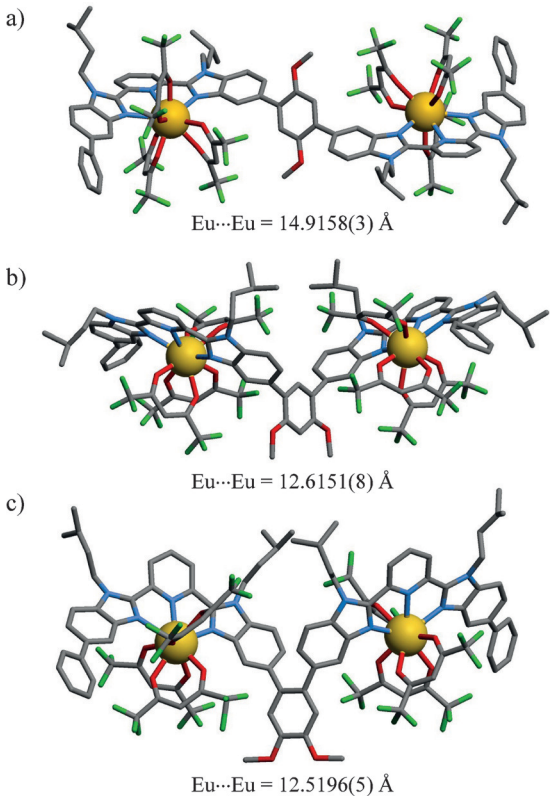

Figure 7. Molecular structures of: a) [**L2a**Eu$_2$(hfac)$_6$], b) [**L3a**Eu$_2$(hfac)$_6$], and c) [**L4a**Eu$_2$(hfac)$_6$] found in the crystal structures of **6**–**8**. The intramolecular Eu···Eu distances are highlighted. Color codes: C = grey, N = blue, O = red, F = green, Eu = orange. The hydrogen atoms are omitted for clarity.

Each tridentate binding units in **L0** or in **L2**–**L4** adopts a *trans–trans* arrangement of the nitrogen atoms bearing the lone pairs,[45] thus leading to weak local dipole moments of 1.7 D, mainly oriented along the C_{para}–N direction of the pyridine ring (Figure 8a). Depending on the relative orientation of the two terminal tridentate binding units in the dimers **L2**–**L4** (Figure S12, left column), the total dipole moments slightly differ from that of the monomer (Figure 8c, column 2 in Table 1). Upon complexation to [Ln(hfac)$_3$], each tridentate binding unit displays a *cis–cis* arrangement compatible with its meridional tricoordination to nine-coordinate europium cations as found in the molecular structures of [**L0**La(hfac)$_3$][41] and [**Lk**Eu$_2$(hfac)$_6$] (**Lka** = **L2a**–**L4a** and **L2**), the six remaining positions around each metal being occupied by the three didentate hexafluoroacetylacetonate ligands (Figure 7). A SHAPE[64] analysis shows that the geometries of the EuN$_3$O$_6$ coordination spheres can be described either as tricapped trigonal prisms or as monocapped square antiprisms. All bond lengths and bond angles are standard (Table S25 in the Supporting Information).[65] The lack of specific constraints in the molecular structures of the dinuclear complexes is supported by their unresponsiveness to the increasing length of the central alkoxy groups in going from [**L2a**Eu$_2$(hfac)$_6$]·(**6**) to [**L2**Eu$_2$(hfac)$_6$]·(**9**; Figure S13) or to the replacement of Ln = Eu in [**L2**Eu$_2$(hfac)$_6$]·(**9**) with Ln = Er in [**L2**Er$_2$(hfac)$_6$]·(**10**; Figure S14). The dipole moments of 14.2(6) D computed for the monomeric

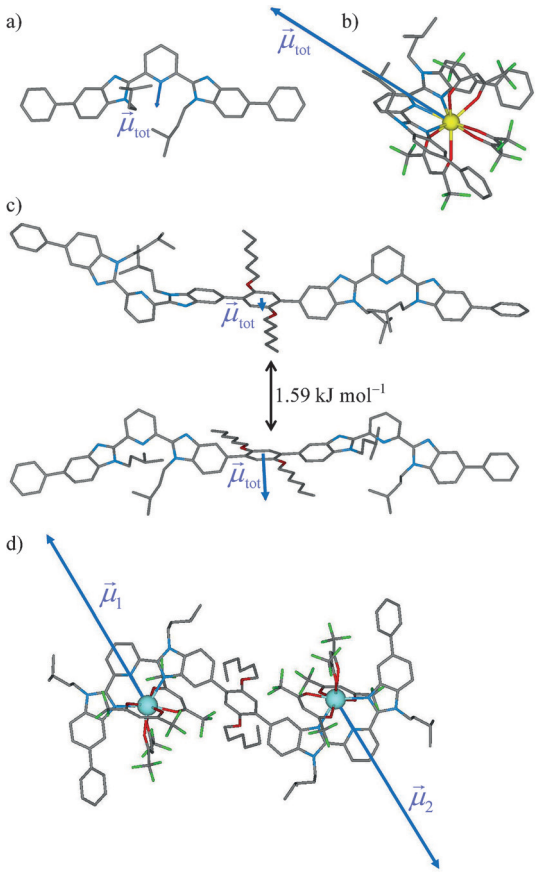

Figure 8. Dipole moments computed for: a) **L0**, b) [**L0**Eu(hfac)$_3$], c) **L2** in its two stable conformations accessible at room temperature with the energy gap between them, and d) "local" dipole moments $\vec{\mu}_1$ and $\vec{\mu}_2$ (computed for each [**L0**Y(hfac)$_3$] separately, see text) represented in the dinuclear complex [**L2**Y$_2$(hfac)$_6$]. All molecular structures correspond to DFT-optimized gas-phase geometries.

complexes [**L0**Ln(hfac)$_3$] (Ln = La, Eu, Y) are almost superimposable (Figure S15) and roughly oriented along the C_{para}–N direction of the central pyridine ring, but pointing in the opposite direction as that found for the uncoordinated ligand (Figure 8a and b). Finally, the dipole moments of the mononuclear [**Lk**Eu(hfac)$_3$] (**Lk** = **L3a**–**L4a**) and dinuclear [**Lk**Eu$_2$(hfac)$_6$] (**Lk** = **L3a**–**L4a**) complexes were estimated by the vectorial sums of the individual dipole moments located of each tridentate binding part of the dimeric ligands (Figure S12 center and right parts). Because of intermetallic distances larger than 1 nm in the dinuclear complexes [**Lk**Ln$_2$(hfac)$_6$], the intersite dipole–dipole interactions computed in the gas phase for estimating $\Delta E^{Ln,Ln}_{1-2,gas}$ [Eq. (8), Table 1, column 5] negligibly contribute (< 5%) to the overall cooperativity index $\Delta E^{Ln,Ln}_{1-2,sol}$ observed in solution [Eq. (7), Table 1 column 7]. The latter parameter is thus controlled by the sum of the solvation energies. At our rough level of approximation for estimating the solvation energies,[60] we cannot expect to satisfyingly reproduce the magnitude of the experimental cooperativity factors, but we note that the stepwise turning away from centrosymmetry along the series *para*-(**L2**)→*meta*-(**L3**)→*ortho*-(**L4**) produces a stepwise increase in the total dipole moments (Table 1, column 2), hence in the solvation energies of the dinuclear complexes ($\Delta_{solv}G^0_{LkLn_2}$, column 6). Consequently, this parameter becomes dominant for the less symmetrical ligand **L4**, and Equation (7) predicts positive cooperativity for the metal loading of **L4** (Table 1, column 7), in agreement with the experimental trend depicted in Figure 5a.

Beyond allosteric cooperativity: the origin of variable intrinsic affinities in metallopolymers

This is a common procedure in chemistry and biology to deduce the cooperativity factor $u^{Ln,Ln}_{1-2} = \beta^{Ln,Lk}_{cond,2} \Big/ \left(f^{Ln,Lk}_{aff,cond}\right)^2$ [Eq. (4)] from the experimental global stability constants $\beta^{Ln,Lk}_{cond,2}$ determined for the saturated receptor in [**Lk**Ln$_2$(hfac)$_6$], while the intrinsic affinity $f^{Ln,Lk}_{aff,exch}$ of each site is taken as the stability constant measured for the monomeric model [**L0**Ln(hfac)$_3$] ($f^{Ln,Lk}_{aff,exch} = \beta^{Ln,L0}_{cond,1}$).[36,56,57] The significant dependence observed in Figure 5b for the intrinsic exchange affinity $f^{Ln,Lk}_{aff,exch}$ along the series [**L0**Ln(hfac)$_3$] →[**L2**Ln(hfac)$_3$]→[**L1**^{N}Ln(hfac)$_3$] casts doubt on this practice. For instance, the introduction of $f^{Ln,L0}_{aff,exch}$ measured for the monomer **L0** into Equation (4) predicts $u^{La,La}_{1-2}$ = 0.26, $u^{Eu,Eu}_{1-2}$ = 0.21 and $u^{Y,Y}_{1-2}$ = 0.55 for the saturated dinuclear complexes [**L2**Ln$_2$(hfac)$_6$], values which deviate by, respectively, 73, 88 and 66% from their correct estimations fixed at $u^{La,La}_{1-2}$ = 0.97(6), $u^{Eu,Eu}_{1-2}$ = 1.7(1) and $u^{Y,Y}_{1-2}$ = 1.64(6) when the absolute affinity found in the dimer $f^{Ln,L2}_{aff,exch}$ [Eq. (3)] is taken as a pertinent reference (Figure S16). The latter drift becomes really dramatic for the metallopolymers [**L1**^{N}Ln$_m$(hfac)$_{3m}$], where allosteric cooperativity factors over-estimated by more than two orders of magnitude are obtained when using the standard method relying on $f^{Ln,L0}_{aff,exch}$ as the reference for the intrinsic affinity (Figure S17). In order to ensure reliable quantitative analyses of cooperativity in chemistry and biology, the origin and control of the dependence of the intrinsic affinity on the number of available sites should be rationalized for being used as a general model for any multiple successive intermolecular associations. The thermodynamic cycle depicted in Scheme 4 and summarized in Equation (10), shows that the free energy of ligand-exchange process $\Delta G^{L0\rightarrow L1^N}_{exch}$ only depends on the ratio of the intrinsic exchange affinities measured in the monomer $f^{Ln,L0}_{aff,exch}$ and in the polymer $f^{Ln,L1^N}_{aff,exch}$ [Eq. (11)].

$$\begin{array}{ccccc} \mathbf{L0}_{gas} & + & [\mathbf{L1}^N\mathrm{Ln(hfac)_3}]_{gas} & \xrightarrow{\Delta G^{L0\rightarrow L1^N}_{exch,gas}} & \mathbf{L1}^N{}_{gas} + [\mathbf{L0}\mathrm{Ln(hfac)_3}]_{gas} \\ \downarrow \Delta_{solv}G^0_{L0} & & \downarrow \Delta_{solv}G^0_{L1^N Ln} & & \downarrow \Delta_{solv}G^0_{L1^N} \quad \downarrow \Delta_{solv}G^0_{L0Ln} \\ \mathbf{L0}_{sol} & + & [\mathbf{L1}^N\mathrm{Ln(hfac)_3}]_{sol} & \xrightarrow{\Delta G^{L0\rightarrow L1^N}_{exch,sol}} & \mathbf{L1}^N{}_{sol} + [\mathbf{L0}\mathrm{Ln(hfac)_3}]_{sol} \end{array}$$

Scheme 4. Thermodynamic cycle for ligand exchange on a [Ln(hfac)$_3$] metal complex.

Reasonably assuming that the gas-phase intrinsic affinities of the tridentate binding unit in **L0** and in the rather rigid polymer **L1**^{N} are comparable, that is, $f^{Ln,L0}_{aff,exch,gas} = f^{Ln,L1^N}_{aff,exch,gas}$,[42] the introduction of Equation (11) into Equation (10) provides the searched dependence of the solution-phase intrinsic affinity

$f_{aff,exch,sol}^{Ln,L1^N}$ of a specific binding site in the polymer $\mathbf{L1}^N$ on the affinity $f_{aff,exch,sol}^{Ln,L0}$ of the same binding site in monomer **L0** [Eq. (12)].

$$\Delta G_{exch,gas}^{L0\rightarrow L1^N} - \Delta G_{exch,sol}^{L0\rightarrow L1^N} = \Delta_{solv}G_{L0}^0 - \Delta_{solv}G_{L1^N}^0 + \Delta_{solv}G_{L1^N Ln}^0 - \Delta_{solv}G_{L0Ln}^0 \quad (10)$$

$$\Delta G_{exch}^{L0\rightarrow L1^N} = -RT\ln\left(K_{exch,1}^{Ln,L0}\Big/K_{exch,1}^{Ln,L1^N}\right) = -RT\ln\left(f_{aff,exch}^{Ln,L0}\Big/N\cdot f_{aff,exch}^{Ln,L1^N}\right) \quad (11)$$

$$f_{aff,exch,sol}^{Ln,L1^N} = f_{aff,exch,sol}^{Ln,L0}\cdot e^{-\left[\left(\Delta_{solv}G_{L0}^0 - \Delta_{solv}G_{L1^N}^0 + \Delta_{solv}G_{L1^N Ln}^0 - \Delta_{solv}G_{L0Ln}^0\right)/RT\right]} \quad (12)$$

The combination of Kuhn theory,[66] which correlates the hydrodynamic radius of a linear polymer $\mathbf{L1}^N$ with respect of its monomeric building element **L0**,[67] with Onsager Equation (9) for estimating the solvation free energies is beyond the scope of this work, but it is detailed in Appendix 3 for the interested readers. Altogether, Equation (12) can be approximated by the power law shown in Equation (13), in which the intrinsic affinity $f_{aff,exch,sol}^{Ln,L1^N}$ of one tridentate binding site in the linear polymer $\mathbf{L1}^N$ is correlated with the intrinsic affinity $f_{aff,exch,sol}^{Ln,L0}$ measured in the monomer.

$$f_{aff,exch,sol}^{Ln,L1^N} = f_{aff,exch,sol}^{Ln,L0}\cdot N^{\left(\beta\Delta_{solv}G_{L0}^0/RT\right)} \quad (13)$$

The argument of the power law reflects the length of the linear polymer $\mathbf{L1}^N$ as estimated by the number of repetitive monomeric binding unit, *N*, while its exponent is controlled by the solvation free energy of the monomer $\Delta_{solv}G_{L0}^0$ weighted by thermal energy *RT*. The empirical and adjustable factor β reflects the influence on solvation energy of the decrease in number of degrees of freedom accompanying the chelate coordination of the binding unit to [Ln(hfac)$_3$] (see Appendix 3 for details). Using $\Delta_{solv}G_{L0}^0 = -0.59\ kJ\,mol^{-1}$ computed for the monomeric ligand **L0** [Eq. (9)], the experimental data collected for the loading of **L2** and $\mathbf{L1}^N$ with [Ln(hfac)$_3$] can be satisfyingly reproduced with the help of Equation (13) by using $\beta_{La} = 2.74$, $\beta_{Eu} = 2.63$ and $\beta_Y = 4.23$, respectively (Figure 6).

Conclusions

The site-binding model depicted in Figure 1b relies on two thermodynamic descriptors, the intrinsic binding affinity $f_{aff}^{M,L} = \exp\left(-\Delta G_{aff}^{M,L}/RT\right)$ and the cooperativity factor $u_{1-2}^{M,M} = \exp\left(-\Delta E_{1-2}^{M,M}/RT\right)$, which are well-adapted for unravelling allosteric cooperativity operating in multisite receptors assuming that both parameters are determined simultaneously for the same system. Applied to the metal loading of bis-tridentate ligands **L2**–**L4**, positive (**L4**), negligible (**L2**) and negative (**L3**) cooperative loading processes could be evidenced, which apparently depend on the specific orientation of the binding sites in the dinuclear [**Lk**Ln$_2$(hfac)$_6$] complexes. A detailed thermodynamic analysis assigns the dominant contribution to solvation processes (> 95 %), while the intuitive electrostatic intersite interactions have only minor influence (< 5 %) in the emergence of the cooperative factors. The fact that solvation effects are also responsible for the decrease of the intrinsic affinity of a given binding site in linear metallopolymers is more challenging (Figure 6). If one assumes that the intrinsic affinity measured in the monomeric model complex is pertinent for the related multisite receptors, cooperativity factors overestimated by one to two orders of magnitude can be erroneously deduced. A simplistic additive model predicts a power-law dependence with the number of binding sites in the polymer, the exponent of which depends on: 1) the solvation of the generating monomeric unit, and 2) conformational changes occurring upon complexation (Appendix 3 in the Supporting Information). The latter phenomenon has crucial consequences for getting reliable quantitative estimations of allosteric cooperativities operating in multisite receptors. In this context, we notice that the recurrent report of weak 0.5 to 2.5 allosteric cooperativity factors in metallopolymers[41,42,55] contrasts with much larger cooperativity factors reported for biological receptors, but: 1) biological systems undergo dramatic conformational changes compared with the rotations at one or two bonds found in linear metallopolymers, and 2) the biological allosteric effects are often deduced by comparison with an external monomeric host–guest system.[56,57] As early as in 1935, Pauling considered these points for critically analyzing pioneer works focused on the fixation of dioxygen to hemoglobin.[68] He therefore decided to use the Ising model in order to avoid reliance on an external reference and he was able to get the first reliable cooperativity factors $u_{1-2}^{O2,O2} = 12 \Rightarrow \Delta E_{1-2}^{O2,O2} = -6.4\ kJ\,mol^{-1}$ for an intrinsic affinity of $f_{aff}^{Fe,O2} = 30.3 \Rightarrow \Delta G_{aff}^{Fe,O2} = -8.79\ kJ\,mol^{-1}$.[68] The model was later refined for matching the exact arrangement and reorganization of the four hemes in the protein upon dioxygen binding,[69] but our current set of data collected for metallopolymers should be considered as a booster shot for providing pertinent interpretations of allosteric cooperativity operating in "simple" multisite receptors.[36]

Acknowledgement

This work was supported through grants of the Swiss National Science Foundation.

Keywords: cooperativity · host–guest systems · lanthanides · metallopolymers · solvation

[1] K. Binnemans, *Chem. Rev.* **2009**, *109*, 4283 – 4374.
[2] J. Feng, H. Zhang, *Chem. Soc. Rev.* **2013**, *42*, 387 – 410.
[3] C.-L. Ho, W.-Y. Wong, *Coord. Chem. Rev.* **2011**, *255*, 2469 – 2502.
[4] B. Happ, A. Winter, M. D. Hager, U. S. Schubert, *Chem. Soc. Rev.* **2012**, *41*, 2222 – 2255.
[5] J. M. Stanley, B. J. Holliday, *Coord. Chem. Rev.* **2012**, *256*, 1520 – 1530.
[6] J. Kido, Y. Okamoto, *Chem. Rev.* **2002**, *102*, 2357 – 2368.
[7] B. S. Harrison, T. J. Foley, A. S. Knefely, J. K. Mwaura, G. B. Cunningham, T.-S. Kang, M. Bouguettaya, J. M. Boncella, J. R. Reynolds, K. S. Schanze, *Chem. Mater.* **2004**, *16*, 2938 – 2947.
[8] M. A. Katkova, M. N. Bochkarev, *Dalton Trans.* **2010**, *39*, 6599 – 6612.
[9] A. de Bettencourt-Dias, *Dalton Trans.* **2007**, 2229 – 2241.
[10] X. Huang, S. Han, W. Huang, X. Liu, *Chem. Soc. Rev.* **2013**, *42*, 173 – 201.

[11] J.-C. G. Bünzli, A.-S. Chauvin, in *Handbook on the Physics and Chemistry of Rare Earths, Vol. 44* (Eds.: J.-C. G. Bünzli, V. K. Pecharsky), Elsevier, Amsterdam, **2014**, pp. 169 – 281.
[12] Y. Hasegawa, *Bull. Chem. Soc. Jpn.* **2014**, *87*, 1029 – 1057.
[13] K. Binnemans, R. van Deun, C. Görller-Walrand, W. Haase, D. W. Bruce, L. Malykhina, Y. G. Galyametdinov, *Mater. Sci. Eng.* **2001**, *18*, 247 – 254.
[14] C. Piguet, J.-C. G. Bünzli, B. Donnio, D. Guillon, *Chem. Commun.* **2006**, 3755 – 3768.
[15] K. Binnemans, in *Handbook on the Physics and Chemistry of Rare Earths*, Vol. 43 (Eds.: J.-C. G. Bünzli, V. K. Pecharsky), Elsevier, Amsterdam, **2013**, pp. 1 – 158.
[16] K. Kuriki, Y. Koike, Y. Okamoto, *Chem. Rev.* **2002**, *102*, 2347 – 2354.
[17] L. H. Sloof, A. van Blaaderen, A. Polman, G. A. Hebbink, S. I. Klink, F. C. J. M. Van Veggel, D. N. Reinhoudt, J. W. Hofstraat, *J. Appl. Phys.* **2002**, *91*, 3955 – 3980.
[18] R. Shunmugam, G. N. Tew, *J. Am. Chem. Soc.* **2005**, *127*, 13567 – 13572.
[19] A. Balamurugan, M. L. P. Reddy, M. Jayakannan, *J. Phys. Chem. B* **2011**, *115*, 10789 – 10800.
[20] M. O. Wolf, *Adv. Mater.* **2001**, *13*, 545 – 553.
[21] N. L. Rosi, M. Eddaoudi, J.-J. Kim, M. O'Keefe, O. M. Yaghi, *CrystEngComm* **2002**, *4*, 401 – 404.
[22] T. R. Cook, Y.-R. Zheng, P. J. Stang, *Chem. Rev.* **2013**, *113*, 734 – 777.
[23] J. Heine, K. Müller-Buschbaum, *Chem. Soc. Rev.* **2013**, *42*, 9232 – 9242.
[24] Y. Cui, Y. Yue, G. Qian, B. Chen, *Chem. Rev.* **2012**, *112*, 1126 – 1162.
[25] A. Duerrbeck, S. Gorelik, J. Hobley, J. Wu, A. Hor, N. Long, *Chem. Commun.* **2015**, *51*, 8656 – 8659.
[26] P. Chen, Q.-S. Li, S. Grindy, N. Holten-Andersen, *J. Am. Chem. Soc.* **2015**, *137*, 11590 – 11593.
[27] K. A. White, D. A. Chengelis, K. A. Gogik, J. Stehman, N. L. Rosi, S. Petoud, *J. Am. Chem. Soc.* **2009**, *131*, 18069 – 18071.
[28] F. Le Natur, G. Calvez, C. Daiguebonne, O. Guillou, K. Bernot, J. Ledoux, L. Le Pollès, C. Roiland, *Inorg. Chem.* **2013**, *52*, 6720 – 6730.
[29] D. R. Kauffman, C. M. Shade, H. Uh, S. Petoud, A. Star, *Nat. Chem.* **2009**, *1*, 500 – 506.
[30] S. J. Bradberry, A. J. Savyasachi, M. Martinez-Calvo, T. Gunnlaugsson, *Coord. Chem. Rev.* **2014**, *273 – 274*, 226 – 241.
[31] M. C. Heffern, L. M. Matosziuk, T. J. Meade, *Chem. Rev.* **2014**, *114*, 4496 – 4539.
[32] S. Floquet, N. Ouali, B. Bocquet, G. Bernardinelli, D. Imbert, J.-C. G. Bünzli, G. Hopfgartner, C. Piguet, *Chem. Eur. J.* **2003**, *9*, 1860 – 1875.
[33] D. A. Turchetti, M. M. Nolasco, D. Szczerbowski, L. D. Carlos, L. C. Akcelrud, *Phys. Chem. Chem. Phys.* **2015**, *17*, 26238 – 26248.
[34] L. Aboshyan-Sorgho, C. Besnard, P. Pattison, K. R. Kittilstved, A. Aebischer, J.-C. G. Bünzli, A. Hauser, C. Piguet, *Angew. Chem. Int. Ed.* **2011**, *50*, 4108 – 4112; *Angew. Chem.* **2011**, *123*, 4194 – 4198.
[35] G. Koper, M. Borkovec, *J. Phys. Chem. B* **2001**, *105*, 6666 – 6674.
[36] G. Ercolani, L. Schiaffino, *Angew. Chem. Int. Ed.* **2011**, *50*, 1762 – 1768; *Angew. Chem.* **2011**, *123*, 1800 – 1807.
[37] M. Borkovec, J. Hamacek, C. Piguet, *Dalton Trans.* **2004**, *4096* – 4105.
[38] M. S. Rocha, *Integr. Biol.* **2015**, *7*, 967 – 986.
[39] N. Dalla Favera, J. Hamacek, M. Borkovec, D. Jeannerat, G. Ercolani, C. Piguet, *Inorg. Chem.* **2007**, *46*, 9312 – 9322.
[40] M. Borkovec, G. J. M. Koper, C. Piguet, *Curr. Opin. Colloid Interface Sci.* **2006**, *11*, 280 – 289.
[41] L. Babel, T. N. Y. Hoang, H. Nozary, J. Salamanca, L. Guénée, C. Piguet, *Inorg. Chem.* **2014**, *53*, 3568 – 3578.
[42] T. N. Y. Hoang, Z. Wang, L. Babel, H. Nozary, M. Borkovec, I. Szilagyi, C. Piguet, *Dalton Trans.* **2015**, *44*, 13250 – 13260.
[43] G. J. M. Koper, M. Borkovec, *Polymer* **2010**, *51*, 5649 – 5662.
[44] R. G. Smits, G. J. M. Koper, M. Mandel, *J. Phys. Chem.* **1993**, *97*, 5745 – 5751.
[45] J.-F. Lemonnier, L. Guénée, C. Beuchat, T. A. Wesolowski, P. Mukherjee, D. H. Waldeck, K. A. Gogik, S. Petoud, C. Piguet, *J. Am. Chem. Soc.* **2011**, *133*, 16219 – 16234.
[46] W. J. Evans, D. G. Giarikos, M. A. Johnston, M. A. Greci, J. W. Ziller, *J. Chem. Soc. Dalton Trans.* **2002**, 520 – 526.
[47] G. Malandrino, R. Lo Nigro, I. L. Fragalà, C. Benelli, *Eur. J. Inorg. Chem.* **2004**, 500 – 509.
[48] a) M. C. Burla, R. Caliandro, M. Camalli, B. Carrozzini, G. L. Cascarano, L. De Caro, C. Giacovazzo, G. Polidori, D. Siliqi, R. Spagna, *J. Appl. Crystallogr.* **2007**, *40*, 609 – 613; b) SIR97: A. Altomare, M. C. Burla, M. Camalli, G. Cascarano, C. Giacovazzo, A. Guagliardi, G. Moliterni, G. Polidori, R. Spagna, *J. Appl. Crystallogr.* **1999**, *32*, 115 – 119.
[49] G. M. Sheldrick, *Acta Crystallogr. Sect. A* **2008**, *64*, 112 – 122.
[50] O. V. Dolomanov, L. J. Bourhis, R. J. Gildea, J. A. K. Howard, H. Puschmann, *J. Appl. Crystallogr.* **2009**, *42*, 339 – 341.
[51] ORTEP3 for Windows: L. J. Farrugia, *J. Appl. Crystallogr.* **1997**, *30*, 565.
[52] S. Grimme, *J. Comput. Chem.* **2006**, *27*, 1787 – 1799.
[53] a) O. Treutler, R. Ahlrichs, *J. Chem. Phys.* **1995**, *102*, 346 – 354; b) M. V. Arnim, R. Ahlrichs, *J. Chem. Phys.* **1999**, *111*, 9183 – 9190; c) F. Weigend, R. Ahlrichs, *Phys. Chem. Chem. Phys.* **2005**, *7*, 3297 – 3305.
[54] TURBOMOLE V6.6 2014, a development of University of Karlsruhe and Forschungszentrum Karlsruhe GmbH, **1989 – 2007**, TURBOMOLE GmbH, since **2007**; available from http://www.turbomole.com.
[55] T. Riis-Johannessen, N. Dalla Favera, T. K. Todorova, S. M. Huber, L. Gagliardi, C. Piguet, *Chem. Eur. J.* **2009**, *15*, 12702 – 12718.
[56] A. Cornish-Bowden, *FEBS J.* **2014**, *281*, 621 – 632.
[57] S. J. Edelstein, N. Le Novere, *J. Mol. Biol.* **2013**, *425*, 1424 – 1432.
[58] L. Onsager, *J. Am. Chem. Soc.* **1936**, *58*, 1486 – 1492.
[59] D. V. Matyushov, *J. Chem. Phys.* **2004**, *120*, 1375 – 1382.
[60] C. J. Cramer, D. G. Truhlar, *Acc. Chem. Res.* **2008**, *41*, 760 – 768.
[61] *Physical Chemistry*, 9th ed. (P. Atkins, J. de Paula), W. H. Freeman and Company, New York, **2010**, p. 654.
[62] The dipole moments computed for [**L2**Eu$_x$(hfac)$_{3x}$] ($x = 1$–2) using the geometry found in the crystal structure are in line with those obtained for the gas-phase DFT-optimized geometries for [**L2**Y$_x$(hfac)$_{3x}$] ($x = 1$–2; Table S24).
[63] The hydrodynamic radii R_i are deduced from the Connolly volumes ($R_i = \sqrt[3]{3V_{\text{Connolly}}/4\pi}$), which were obtained from the building of the Connolly surface around the molecular structures of ligands or complexes computed in the gas-phase or observed in their crystal structure, and by using a probe radius of 2.4 Å for modeling dichloromethane solvent molecules. see: a) M. L. Connolly, *Science* **1983**, *221*, 709 – 713; b) M. L. Connolly, *J. Appl. Crystallogr.* **1983**, *16*, 548 – 558.
[64] SHAPE is a free software developed by M. Llunell, D. Casanova, J. Cirera, P. Alemany, S. Alvarez, and available online at http://www.ee.ub.edu/. For more information see: a) M. Pinsky, D. Avnir, *Inorg. Chem.* **1998**, *37*, 5575 – 5582; b) D. Casanova, J. Cirera, M. Llunell, P. Alemany, D. Avnir, S. Alvarez, *J. Am. Chem. Soc.* **2004**, *126*, 1755 – 1763; c) J. Cirera, E. Ruiz, S. Alvarez, *Chem. Eur. J.* **2006**, *12*, 3162 – 3167.
[65] A. Zaïm, H. Nozary, L. Guénée, C. Besnard, J.-F. Lemonnier, S. Petoud, C. Piguet, *Chem. Eur. J.* **2012**, *18*, 7155 – 7168.
[66] W. Kuhn, *Kolloid Z.* **1934**, *68*, 2 – 15.
[67] I. Teraoka, *Polymer Solutions*, Wiley, Hoboken, **2002**.
[68] L. Pauling, *Proc. Natl. Acad. Sci. USA* **1935**, *21*, 186 – 191.
[69] A. S. Mahadevi, G. N. Sastry, *Chem. Rev.* **2016**, *116*, 2775 – 2825.

Received: February 23, 2016
Published online on May 3, 2016